GDCh

Research Articles

Angewandte
Chemie
International Edition
www.angewandte.org

Light-Emitting Electrochemical Cells

Binuclear Copper(I) Complexes for Near-Infrared Light-Emitting Electrochemical Cells

Abdelaziz Jouaiti,* Lavinia Ballerini, Hsiang-Ling Shen, Ronan Viel, Federico Polo,
Nathalie Kyritsakas, Stefan Haacke, Yu-Ting Huang, Chin-Wei Lu, Christophe Gourlaouen,
Hai-Ching Su,* and Matteo Mauro*

Abstract: Two binuclear heteroleptic Cu^I complexes, namely Cu–NIR1 and Cu–NIR2, bearing rigid chelating diphosphines and π-conjugated 2,5-di(pyridin-2-yl)thiazolo[5,4-*d*]thiazole as the *bis*-bidentate ligand are presented. The proposed dinuclearization strategy yields a large bathochromic shift of the emission when compared to the mononuclear counterparts (M1–M2) and enables shifting luminescence into the near-infrared (NIR) region in both solution and solid state, showing emission maximum at ca. 750 and 712 nm, respectively. The radiative process is assigned to an excited state with triplet metal-to-ligand charge transfer (^{3}MLCT) character as demonstrated by in-depth photophysical and computational investigation. Noteworthy, X-ray analysis of the binuclear complexes unravels two interligand π–π-stacking interactions yielding a doubly locked structure that disfavours flattening of the tetrahedral coordination around the Cu^I centre in the excited state and maintain enhanced NIR luminescence. No such interaction is present in M1–M2. These findings prompt the successful use of Cu–NIR1 and Cu–NIR2 in NIR light-emitting electrochemical cells (LECs), which display electroluminescence maximum up to 756 nm and peak external quantum efficiency (EQE) of 0.43 %. Their suitability for the fabrication of white-emitting LECs is also demonstrated. To the best of our knowledge, these are the first examples of NIR electroluminescent devices based on earth-abundant Cu^I emitters.

Introduction

Light-emitting electrochemical cells (LECs) are appealing optoelectronic devices due to their potential application in low-cost, large-area display technology and disposable devices.[1] Ionic transition metal complexes (iTMCs) are typically employed as electroluminescent materials in LECs, particularly cyclometalated Ir^{III}-based iTMCs.[2] More recently, earth-abundant metals became the subject of intensive research,[3] being Cu^I-based emitters with d^{10} electronic configuration considered an attractive alternative.[4] To date, Cu^I complexes with either mononuclear,[5] binuclear,[6] or multinuclear[7] scaffolds have been investigated, which displays luminescence spanning from the blue to the orange spectral region. Designing complexes that efficiently emit into the deep-red to near-infrared (NIR) region is still highly challenging and examples of Cu^I derivatives are still very rare.[8]

The difficulty stems from a three-fold reason: *i*) the smaller spin orbit coupling (SOC) constant of copper

[*] Dr. A. Jouaiti
Laboratoire de Synthèse et Fonctions des Architectures Molécu-laires, UMR7140 Chimie de la Matiere Complexe, Université de Strasbourg & CNRS
4 rue Blaise, Pascal 67000 Strasbourg (France)
E-mail: jouaiti@unistra.fr

L. Ballerini, R. Viel, Prof. Dr. S. Haacke, Dr. M. Mauro
Institut de Physique et Chimie des Matériaux de Strasbourg (IPCMS) UMR7504, Université de Strasbourg & CNRS
23 rue du Loess, 67083 Strasbourg (France)
E-mail: mauro@unistra.fr

H.-L. Shen, Prof. Dr. H.-C. Su
Institute of Lighting and Energy Photonics, National Yang Ming Chiao Tung University
Tainan 71150 (Taiwan)
E-mail: haichingsu@nycu.edu.tw

Prof. Dr. F. Polo
Department of Molecular Sciences and Nanosystems, Ca' Foscari University of Venice
Via Torino 155, 30172 Venezia (Italy)

N. Kyritsakas
Service de Radiocristallographie, Fédération de chimie Le Bel – FR2010, Université de Strasbourg & CNRS
1, rue Blaise Pascal, 67008 Strasbourg (France)

Y.-T. Huang, Prof. Dr. C.-W. Lu
Department of Applied Chemistry, Providence University
Taichung 43301 (Taiwan)

Dr. C. Gourlaouen
Laboratoire de Chimie Quantique, Institut de Chimie de Strasbourg UMR7177, Université de Strasbourg & CNRS
4 Rue Blaise Pascal, 67008 Strasbourg (France)

compared to iridium and platinum ($\zeta_{Cu} = 857$ cm^{-1}; $\zeta_{Ir} = 3909$ cm^{-1}; $\zeta_{Pt} = 4481$ cm^{-1}) yields complexes with slower radiative rate constant (k_r);[9] *ii*) given the third-power dependency with emission energy, as by Einstein's theory of spontaneous emission, red to NIR emitters possess intrinsically smaller k_r; *iii*) efficient non-radiative vibronic coupling between T_1 and ground state is at play (*energy gap law*).

NIR emitters are very appealing for the fabrication of light-emitting devices for night vision display, optical telecommunication technology, biomedical devices for phototherapy.[10] Costa and co-workers reported on deep-red emitting mononuclear heteroleptic Cu^I complexes [Cu-(P^P)(N^N)]PF$_6$ bearing a 4,4′-diethylester-2,2′-biquinoline ligand as the N^N ligand, and mono- and diphosphines. LECs fabricated with these emitters provided electroluminescence peaking at $\lambda_{EL} = 675$ nm.[11] Cu^I complexes that emit beyond 700 nm and that were also employed as active materials in light-emitting devices is unprecedented, to the best of our knowledge.

Recently, bi- and multi-nuclear complexes appeared to be a valuable strategy for the preparation of deep-red to NIR emitters.[12] Herein, we describe a dinuclearization strategy in heteroleptic copper complexes to achieve NIR emission. The compounds bear a π-extended thiazolo[5,4-*d*]thiazole (TzTz) scaffold that acts as the bridging *bis*-bidentate chromophoric ligand, whereas P^P is a chelating diphosphine. Remarkably, NIR electroluminescence (EL) is demonstrated for the first time with λ_{EL} maximum up to 756 nm when the investigated binuclear complexes are employed as emitters in LEC devices.

Results and Discussion

Synthesis and characterization

The chemical structure of the investigated binuclear Cu^I complexes and their mononuclear counterparts is depicted in Figure 1. Full details on the synthetic procedures along with the chemical characterization of all the intermediates and final compounds are provided in the Supporting Information (see Scheme S1–S2, Figure S1–S21 and Supplementary procedure). Complex Cu–NIR1 and Cu–NIR2 possess general formula [Cu(P^P)(L1)Cu(P^P)](PF$_6$)$_2$, where L1 is a 2,5-di(pyridin-2-yl)thiazolo[5,4-*d*]thiazole (TzTz) scaffold acting as bridging *bis*-bidentate chromophoric ligand, and P^P is the chelating *bis*[(2-diphenylphosphino)phenyl]ether (DPEPhos) and 4,5-*bis*(diphenylphosphino)-9,9-dimethylxanthene (XantPhos), respectively. The mononuclear complexes have general formula [Cu(P^P)(L2)]PF$_6$, namely M1 and M2 for P^P = DPEPhos and XantPhos, respectively, where ligand L2 is 2-(5-(3,5-di-*tert*-butylphenyl)pyridin-2-yl)benzo[*d*]thiazole.
The synthesis of these latter follows an adapted version of a procedure reported elsewhere.[8a] Complexation reaction afforded the target compounds in high yields.

The structure of ligand L1 as well as all the four investigated complexes have been established by single crystal X-ray diffractometric analysis and the ORTEP
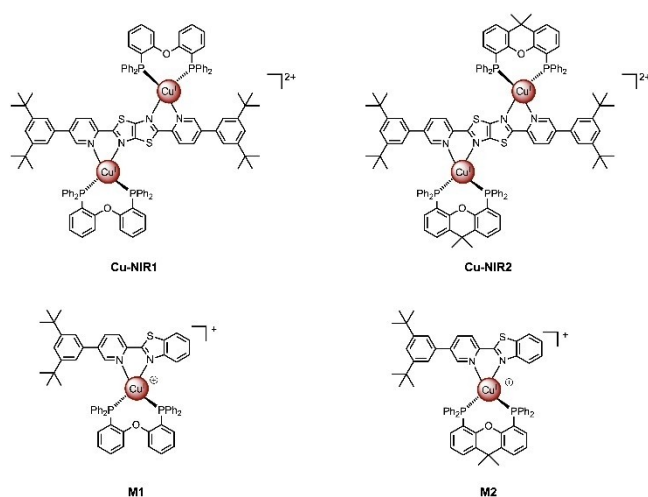

Figure 1. Chemical structure of the dinuclear complexes Cu–NIR1 and Cu–NIR2 along with their mononuclear M1 and M2 counterparts. All the compounds were prepared as PF$_6^-$ salt.

diagrams of Cu–NIR2 and 4, M1, M2 and Cu–NIR1 are displayed in Figure 2 and S22–S25, respectively (see Table S1–S5 for crystallographic parameters).[13] The structure of the complexes agrees with those reported previously for related compounds, showing the coordination of the Cu^I ion in a distorted tetrahedral environment and for binuclear Cu–NIR1 and Cu–NIR2 derivatives confirmed their bimetallic nature as well.[5,14] The four coordination sites of each Cu^I ion are occupied by the chelating P^P ligand and two nitrogen atoms of the 2,5-di(pyridin-2-yl)thiazolo[5,4-*d*]thiazole, this latter acting as the *bis*-bidentate scaffold.

Minimizing quenching processes is of paramount importance especially for NIR emitters that possess intrinsically lower k_r and high k_{nr} values. Remarkably, two π–π stacking interactions are present between one of the phenyl groups of each of the chelating phosphines and the π-extended ligand L1, where interplanar distance is ca. 3.57 and 3.62 Å, for Cu–NIR1 and Cu–NIR2, respectively (see Figure 2 and S25). The presence of these interactions gives rise to a doubly locked structure that helps mitigate quenching processes such as pseudo-Jahn–Teller distortions and structural flattening typically occurring in the excited state of Cu^I complexes.[5,14,15] Indeed, it has been recently highlighted the fundamental role played by such π-stacking interaction in preserving the emissive properties of mononuclear [Cu-(P^P)(N^N)]$^+$ derivatives.[15] Interligand π-stacking interactions are absent in the monometallic derivatives M1 and M2 instead (see Figure S23–S24).

The compounds possess remarkably high thermal stability under air with $T_{5\%}$, i.e. the temperature at which 5 % of the initial weight loss has occurred, $\geq 300 \,°C$ (see thermogravimetric analysis in Figure S26–S27). Voltammetric investigations in the full width potential window in CH$_2$Cl$_2$/0.1 M tetra-*n*-butylammonium hexafluorophosphate (TBAPF$_6$) are shown in Figure 3 and S28, while a summary of the data is reported in Table 1. In the negative-going scan, either two or three reversible and irreversible reduction processes $R_{i,n}$
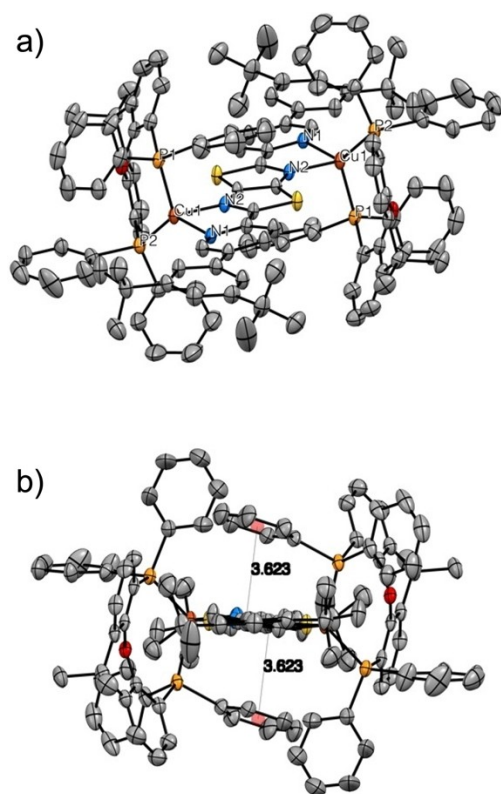
a)

b)

Figure 2. ORTEP diagram of compound Cu–NIR2 with thermal ellipsoids shown at 50% probability level obtained by single-crystal X-ray diffractometric analysis along two different views (box a and b). Right view highlights the interligand π-stacking interactions involving phosphines and the TzTz ligand. Hydrogen atoms, PF_6^- anions and solvent molecules are omitted for clarity. Selected bond lengths (Å): Cu–N(1)=2.097(5), Cu–N(2)=2.072(4), Cu–P(1)=2.2748(18), Cu–P-(2)=2.259(19). Selected bond angles (°): N(1)–Ir–N(2)=79.52(18), P(1)–Ir–P(2)=124.53(6).

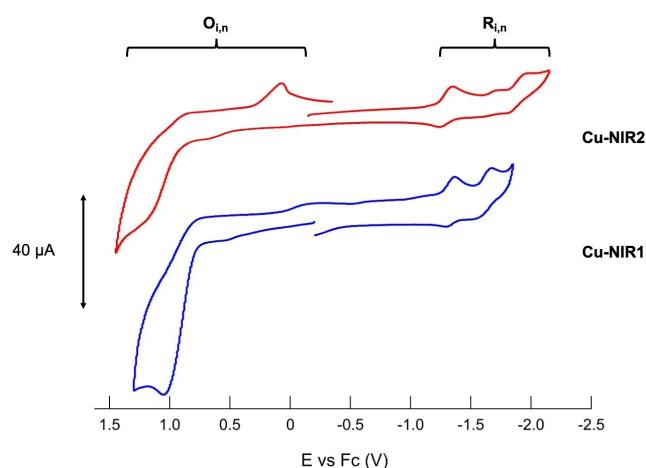**Figure 3.** CV recorded for copper complexes Cu–NIR1 (blue curve) and Cu–NIR2 (red curve) at concentration of 1 mM and carried out in CH_2Cl_2/0.1 M TBPF$_6$. Scan rate 0.2 V s^{-1}.

(where i denotes the investigated binuclear or mononuclear compounds and n the process number) occurred in the

potential range from −1.2 V to −2.2 V. In particular, the process $R_{i,1}$, which is common to both bimetallic complexes, shows a clear reversibility at all the investigated scan rates (0.05–0.5 V/s). This process is more likely associated to the reduction of the π-accepting ligand L1 coordinated onto the two Cu^I centres.[8a] L1 was also investigated and showed indeed two reduction processes, a reversible $R_{L1,1}$ at −2.02 V and an irreversible $R_{L1,2}$ at −2.38 V vs Fc (see Figure S28). Whereas, $R_{i,2–3}$ are irreversible, although $R_{Cu-NIR2,2}$ seems to show some reversibility at scan rate higher than 0.2 V s^{-1}.

In the positive-going scan, the binuclear complexes showed a very weak process around 0.5 V vs Fc and a main irreversible oxidation process, $O_{i,1}$, whose peak potential $E_{p,O_{i,1}}$ is at about +1.07 V vs Fc for Cu–NIR1, whereas it is not well defined, but above 1.1 V vs Fc for Cu–NIR2. The latter also showed an irreversible cathodic peak at about 0.08 V vs Fc, which appeared only when scanning the potential toward very positive values (ca. 1.5 V) before reverting the scan direction and it is most likely due to irreversible oxidation products. L1 did not show any process in the positive-going scan. Therefore, we can attribute the $O_{i,1–2}$ to the oxidation of the metal center. It is also worth mentioning that limited redox reversibility may represent a drawback for their application in LECs, although one should keep in mind that redox behavior in solid state may differ sharply from that observed in dilute solution. The parent mononuclear complexes, namely M1 and M2, were also investigated to compare the electrochemical pattern of the derived binuclear ones (Figure S28). Both M1 and M2 showed a reversible process $R_{i,1}$ in the negative-going scan at −1.77 and −1.73 V vs Fc, respectively. Similarly, in the positive-going scan another reversible process $O_{i,1}$ occurs at 0.94 and 1.00 V vs Fc, respectively, as shown in Figure S28. It is also worth noting that the peak-to-peak separation for all compound is in the range 80–130 mV (see Table 1), which is larger than expected for an ideal Nernstian behavior (59 mV).[16] However, the behavior of the redox couple ferrocene/ferricenium (Fc$^+$|Fc^0), used as internal standard, showed the same trend. This effect can be attributed to the ohmic drop of the system, despite the feedback correction was applied, as previously observed for aprotic media.[17] Furthermore, by taking into account the diffusion coefficient of Cu–NIR1 and Cu–NIR2 (see supplementary discussion #1 and Figure S29 in the Supporting Information) and by comparing the current intensities of their $R_{1,n}$ and $O_{1,n}$ processes with the oxidation of Fc, one can confidently state that the reduction processes are monoelectronic, whereas oxidations might involve more than one electron.

Photophysical investigation

Firstly, the optical properties of complex Cu–NIR1 and Cu–NIR2 were investigated in dilute (3×10^{-5} M) CH_2Cl_2 solution at room temperature in both air-equilibrated and degassed conditions. The corresponding photophysical data are listed in Table 2 and the absorption and emission spectra are displayed in Figure 4. Figure S30 displays the spectra of pro-ligand L1.

Table 1: Main electrochemical data of complex Cu−NIR1 or Cu−NIR2. CVs were carried out in CH_2Cl_2/0.1 M $TBAPF_6$. The values are referenced to the redox couple ferrocene/ferricenium (Fc|Fc$^+$) as the internal standard.

Compound	$E^0_{O_{n,1}}$ (V) [a]	$\Delta E_{p,O_{n,1}}$ (mV) [b]	$E^0_{R_{n,1}}$ (V) [a]	$\Delta E_{p,R_{n,1}}$ (mV) [b]	$E_{p,R_{n,2}}$ (V)	$E_{p,R_{n,3}}$ (V)	EC_{gap} (eV) [e]	ΔE_{DFT} (eV) [f]
Cu−NIR1	+1.07 [c]	–	−1.33	80	−1.72 [c]	–	2.40	2.90
Cu−NIR2	>1.1 [c,d]	–	−1.29	100	−1.65 [c]	−1.93 [c]	>2.39	2.90
M1	0.94	110	−1.77	93	–	–	2.71	–
M2	1.00	115	−1.73	97	–	–	2.73	–
L2	–	–	−2.02	130	−2.38 [c]	–	–	–

[a] Reversible process. The formal potential, E^0, was calculated as the average of the cathodic and anodic peak of the process. [b] ΔE_p is referred to the scan rate 0.2 V/s. [c] Irreversible processes. Only the peak potential, E_p, is reported. [d] Not well defined. [e] Electrochemical band gap calculated as $E_{O_{n,1}} - E_{R_{n,1}}$, where E is either E^0 or E_p (depending on whether the processes are reversible or not). [f] Computed energy gap (ΔE_{DFT}) is defined as the HOMO–LUMO gap.

Table 2: Photophysical data recorded for complexes NIR–Cu1, NIR–Cu2, M1 and M2 as well as ligand L1 for degassed CH_2Cl_2 sample at both room temperature at concentration of 3×10^{-5} M and in frozen matrix at 77 K. Values in brackets correspond to air-equilibrated samples.

compound	λ_{abs} (ε) [nm, (10^3 M^{-1} cm^{-1})] [a]	λ_{em} [nm] [b]	PLQY (%) [b]	τ [ns] [b]	λ_{em} [nm] [c]	τ [μs] [c]	$E_{0,0}$ [eV] [d]
Cu−NIR1	279*sh*, (41.5) 407, (57.7) 504*sh*, (3.0)	746 [763]	0.13 [0.09]	38.9 (36%) 81.6 (64%) [43.7 (52%) 88.4 (48%)]	627, 686, 758, 842 (sh)	320.6 (72%) 81.6 (28%)	2.13
Cu−NIR2	268, (53.9) 407, (56.6) 500, (3.1)	732 [746]	0.06 [0.03]	15.6 (86%) 8.0 (14%) [14.5]	624, 683,753, 842 (sh)	322.3 (71%) 82.8 (29%)	2.13
M1	260*sh*, (25.9) 284*sh*, (22.2) 352, (28.8) 425*sh*, (3.3)	699 [699]	0.5	318.6 [215.3]	624	39.7 (42%) 398.1 (16%) 139.0 (42%)	2.30
M2	261, (27.8) 278, (28.7) 351, (27.5) 425*sh*, (3.2)	695 [693]	0.6	273.8 [207.9]	621	112.5 (44%) 32.9 (40%) 311.8 (16%)	2.15
L1	253*sh*, (17.9) 289, (12.5) 390, (67.6) 407*sh*, (53.2)	[457]	[38.6]	[0.64]	–	–	2.93

[a] *sh* denotes a shoulder; [b] data recorded in dilute CH_2Cl_2 solution at room temperature; [c] data recorded in frozen CH_2Cl_2 matrix samples at 77 K; [d] $E_{0,0}$ is estimated as the crossing point between absorption and emission spectra.
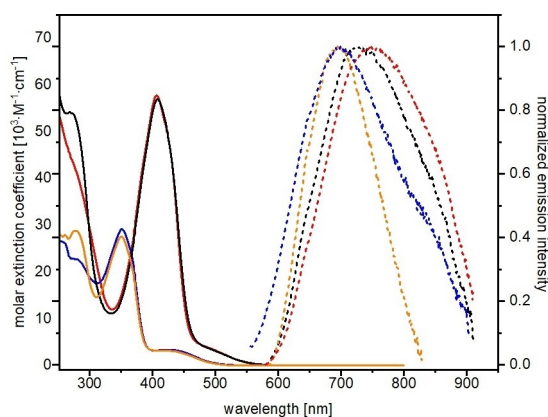

Figure 4. Electronic absorption (solid traces) and emission spectra (dashed traces) of dinuclear complex Cu−NIR1 (red) and Cu−NIR2 (black) and mononuclear M1 (blue) and M2 (orange) Cu^I complexes recorded for CH_2Cl_2 samples at concentration of 3×10^{-5} M at room temperature upon excitation at $\lambda_{exc} = 480$ nm for Cu−NIR1 (red) and Cu−NIR2 and 425 nm for M1 and M2.

As far as the bimetallic complexes Cu−NIR1 and Cu−NIR2 are concerned, their electronic absorption spectrum displays rather similar features that are characterized by three main bands. On the higher energy side, an intense band ($\lambda_{abs} = 280$ nm, $\varepsilon = 4.1\times10^4$ M^{-1} cm^{-1}) is attributable to electronic transitions with singlet-manifold intraligand (^{1}IL) nature involving both the arylphosphines and ligand L1. The intense and narrow band observed at $\lambda_{abs} = 407$ nm ($\varepsilon = 5.8\times10^4$ M^{-1} cm^{-1} for compound Cu−NIR1) can be ascribed with confidence to a metal-perturbed $^1\pi$–π (^{1}IL) absorption mainly localized onto the ligand L1 scaffold, in agreement with the data of this latter. On the lower energy side, the much less intense ($\varepsilon = 5.8\times10^4$ M^{-1} cm^{-1} for compound Cu−NIR1) and broader band can be ascribed to a transition with admixed singlet metal-to-ligand charge transfer (^{1}MLCT) and metal-perturbed ligand-to-ligand charge transfer (^{1}LLCT) with $d\pi$(Cu)$\rightarrow\pi^*_{TzTz}$ and π(aryl-P)$\rightarrow\pi^*_{TzTz}$ character, respectively. Such band is shifted hypsochromically by about 3690 cm^{-1} ($\lambda_{abs} = 425$ nm, $\varepsilon = 3.3\times$

$10^3\,M^{-1}cm^{-1}$) in the corresponding mononuclear derivative M1, whereas it is absent in the spectra of ligand L1, supporting this attribution. Overall, these assignments are made by comparison with the spectrum of L1 (*cf.* Figure S30) as well as related derivatives reported previously,[5,8,15] and are in agreement with computational data (see below).

Upon excitation in the range 400–500 nm, solution samples of both binuclear complexes display broad and featureless NIR photoluminescence at room temperature, with emission centered at $\lambda_{em} = 746$ and 732 nm for derivative Cu–NIR1 and Cu–NIR2, respectively, and photoluminescence quantum yield of 0.13% and 0.06% in degassed conditions. The steady-state emission appeared to be wavelength-independent, but it displayed a slight bathochromic shift in air-equilibrated condition. Upon pulsed ps-laser excitation, excited-state decay traces display a bi-exponential decay with $\tau_1 = 81.6$ (64%) and $\tau_2 = 38.9$ (36%) ns, for derivative Cu–NIR1, and even shorter lifetimes are recorded for the analogues Cu–NIR2 (see Table 2). De-excitation decays were little dependent on the presence of the triplet dioxygen, as expected for a diffusion-controlled quenching process kinetically competing with such a short-living excited state.

Conversely, mononuclear parental complexes M1 and M2 display hypsochromically shifted emission with maximum at $\lambda_{em} = 700$ nm, owing to the much shorter π-conjugation length of the chromophoric ligand, along with a prolonged excited state and higher PLQY, being the values $\tau = 319$ ns and 0.5%, respectively, for M1 in degassed condition, in agreement with the energy gap law. Overall, the bi-exponential decay and the oxygen-dependency observed in the photoluminescence of the binuclear compounds point towards the presence of two energetically close-lying excited states, yet not fully equilibrated on the time scale of the overall radiative processes.

To gain deeper insights into the excited state processes at shorter time scales, the bi- and mono-metallic complexes were studied by picosecond fluorescence spectroscopy based on a streak camera with 10 ps time resolution and operated in photon counting mode. Exemplary data are shown in

Figure 5 for the complex Cu–NIR1 upon $\lambda_{exc} = 515$ nm and acquired for emission wavelengths in the spectral window $\lambda_{em} = 540$–780 nm over different time ranges (1, 50 and 500 ns). The decay kinetics for the other complexes herein investigated are very similar and are summarised in the Figure S31 of the Supporting Information.

Within the first nanosecond, a significant decay by more than 90% of the emission is observed at all wavelengths (Figure 5A). This is in line with the low PLQY of the complex in solution (Table 2). The decay is almost unresolved for wavelengths shorter than 600 nm, but it shows a resolved decay at longer wavelengths on the time scale of a few tens of ps. The remaining weak emission can be better detected at longer time scales when the number of photons per time interval is increased by a factor of 50 or 500, respectively. The data show a strong dependence of the decay times as a function of wavelength. In the 50 ns time range (Figure 5B), one observes a decay of the emission on a time scale of a few ns at <600 nm, while the emission at >600 nm hardly decays within 50 ns. The full decay of the long wavelength emission is captured on a 500 ns time range (Figure 5C). Figure 6 shows exemplary kinetics traces for the three different time ranges and at the emission wavelengths indicated as dotted lines in Figure 6, together with non-linear fits as sum of exponentials convolved by a Gaussian which represents the temporal instrument response function (IRF). The results of the fit give four main time constants, as summarised in Table S6.

These four main decay times are $\tau_1 < 10$ ps, $\tau_2 = 40 \pm 5$ ps, $\tau_3 = 4.0 \pm 0.5$ ns and $\tau_4 = 65 \pm 5$ ns. The value of τ_4 agrees well with the longest lifetime found for this compound by time-correlated single photon counting (TCSPC) technique (see Table 2). Since the amplitudes of the decay times are strongly wavelength-dependent, we performed a global fit, assuming wavelength-independent decay times. This provides the decay associated emission spectra (DAES) for τ_2 to τ_4 (and a longer component τ_5 of negligible amplitude) plotted in Figure S32 of the Supporting Information. In addition to the unresolved τ_1, found to occur only at $\lambda < 600$ nm, we observe that these three lifetimes appear at selected ranges of wavelengths, which guides our assign-
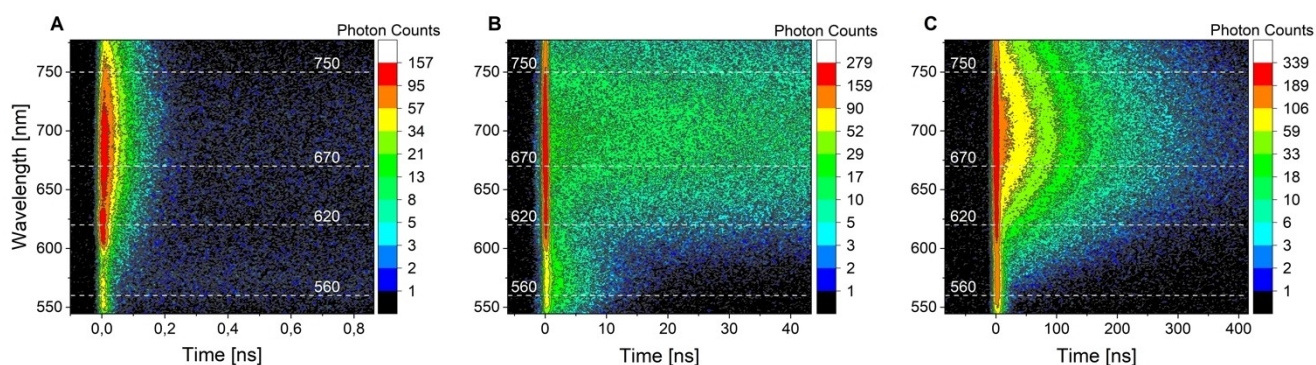

Figure 5. 2D traces recorded for the bimetallic complex Cu–NIR1 for time ranges (A) 1 ns, (B) 50 ns and (C) 500 ns. The white dotted lines stand for the wavelengths of interest i.e. from bottom to top: $\lambda_{em} = 560$, 620, 670 and 750 nm. Data recorded for degassed CH_2Cl_2 samples at concentration of 3×10^{-5} M at room temperature.
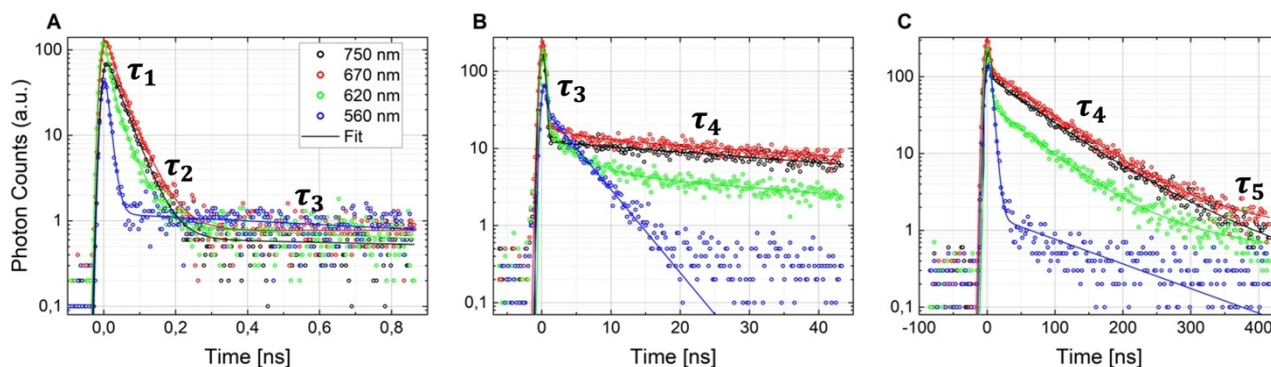
Figure 6. Kinetic traces obtained of complex Cu–NIR1 for time ranges (A) 1 ns, (B) 50 ns and (C) 500 ns.

ments as follows. The longest lifetime τ_4 is with confidence assigned to phosphorescence from an excited triplet state with ^{3}MCLT character. This component largely dominates the steady-state emission spectrum and is detected by TCSPC and its associated DAES agrees well the former (*cf.* Figure 4 and S32). The fact that it slightly shortens in air-equilibrated solution samples confirms the triplet assignment. On the other hand, τ_3 is only observed at shorter wavelengths. Indeed, the DAES associated with τ_3 and τ_4 are clearly separated, indicating that they are related to two different transitions. The 3.5 ns value of τ_3 may suggest that it is due to a highly quenched state that lies at higher energy compared to the ^{3}MCLT manifold. Comparison of the emission spectra observed at 77 K with the DAES associate to τ_3 allow us to rule out the ^{3}LC nature of this latter, which is instead tentatively assigned to a ^{1}LC state (see computational section). Note that this <600 nm component does not show up in the time-averaged fluorescence spectrum due to its short lifetime as compared to τ_4. The lifetime τ_2 is a non-radiative quenching process, most likely related to a flattening and/or geometrical distorsion of the Cu complex, as usually observed for Cu^I under tetrahedral coordination.[18] τ_1, not included in the global fit, is mainly observed in the shortest wavelength range, where the fluorescence emission takes place. It is therefore assigned to intersystem crossing (ISC) process populating the triplet manifolds. But since it is not resolved by the streak camera, it does not show up as a rise time of the phosphorescence.

At 77 K in frozen matrix in CH$_2$Cl$_2$ emission shifts hypsochromically by ca. 2570 cm^{-1} and the appearance of a clear vibronic progression for the binuclear complexes is observed with spacing of ca. 1375 cm^{-1} attributable to the intramolecular C=C and C=N vibrational modes based on related data on thiazolo[5,4-*d*]thiazole organic emitters (Figure S33 and Table 2).[19] The shift is accompanied by a prolongation of the excited-state lifetimes that reach a value as long as $\tau_1 = 320.6$ µs (72%) and $\tau_2 = 81.6$ µs (28%) ($\tau_{average} = 299.0$ µs) for Cu–NIR1. Similar findings are observed for Cu–NIR2. Overall, this effect is indicative of the nature of the emissive excited state that becomes mainly ^{3}LC and is located on the π-conjugated ligand L1. In stark contrast, mononuclear derivatives M1 and M2 retain the broad and featureless emission profile at low temperature

pointing towards a still large ^{3}MLCT character admixed with ^{3}LLCT component of the emitting excited state. Such temperature-dependent data seems to rule out the presence of thermally-activated delayed fluorescence (TADF) processes in dilute solution for these dimetallic derivatives.[8a,15,20] For all the complexes, emission spectra of solid-state samples as neat powder and thin film blends are displayed in Figure S34–S36 of the Supporting Information and the corresponding photophysical data are summarized in Table S7–S8. For both mono- and dinuclear complexes, powder samples show broad and featureless emission profile that is hypsochromically shifted (by ca. 780–1270 cm^{-1}) when compared to fluid solution due to the large CT nature of the emissive excited state and the reduced geometrical relaxation and tendency toward flattening occurring in a more rigid environment such as in the solid state, as previously observed in related mononuclear [Cu(P^P)(N^N)]$^+$ derivatives (*cf.* data in Table 2 and S7–S8).[5,14,15] Interestingly, larger shifts are obtained for mononuclear derivatives M1 and M2 compared to binuclear Cu–NIR1 and Cu–NIR2, indicative of the fact that for the latter geometrical distortion due to environmental effects play a smaller role. Additionally, this spectral shift is accompanied by a prolongation of the excited-state lifetimes that become as long as 3.0–3.5 µs and a remarkable enhancement of PLQY values, which are among the highest for Cu^I emitters in this region.

Computational investigation

Geometrical optimization of pro-ligand L1 and complexes Cu–NIR1 and Cu–NIR2 at their electronic ground state (GS) was carried out by means of density functional theory (DFT). The structure of L1 possesses C_i symmetry and the fused thiazolo[5,4-*d*]thiazole core adopts an almost planar geometry, with $\angle(N_1–C_2–C_3–N_2)$ value of $-13.0°$. Expectedly, the two peripheral phenyl rings are twisted and show $\angle(C_4–C_5–C_6–C_7) = 44.1°$. See Scheme S3 for atom labelling.

Coordination of [Cu(P^P)]$^+$ fragment onto ligand L1 induces large distortions due to multiple π-stacking interactions between the phenyl rings of the diphosphine ligands and the π-extended aromatic scaffold of L1 (see Table S9–

S10 for geometrical parameters). As far as complex Cu–NIR1 at its lowest-energy GS geometry is concerned, four π-stacking interactions are present involving two phenyl rings of each of the two DPEPhos ligands and the thiazolo-[5,4-*d*]thiazole core of L1 and two with the pyridine rings (Figure S37 and Supporting Information Discussion #2). The maximization of these π-stackings leads to a distorted conformation of ligand L1 characterized by a twist of the $N_1–C_2–C_3–N_2$ and $C_4–C_5–C_6–C_7$ dihedral angles by $-23.3°$ (23.8°), an elongation of the Cu–N_1 and Cu–$N_{1'}$ distances by ca. 0.1 Å and an increase of the $\angle(N_1–C_2–C_3–N_2)$ by ca. 20° compared to the values observed in the experimental structure. In complex Cu–NIR2, only two interligand π-stacking interactions are present involving one phenyl ring of each phosphine and the pyridine moiety of ligand L1, owing to the more rigid nature of the diphosphine. The computed structure for Cu–NIR2 agrees well with the experimental one. Overall, a bent geometry of the complex is also observed with M–C_2–C_9 and M–C_2–$C_{9'}$ angles of 156.2° and 160.5°, respectively. Additionally, $N_1–C_2–C_3–N_2$ ($N_1–C_2–C_3–N_{2'}$) dihedral angles of 20.9° ($-10.1°$) are computed, yielding a more distorted structure than that computed for Cu–NIR1, and characterized by rupture of the C_i symmetry. Optimization with C_i constrain yields a less distorted structure that lies 0.250 eV higher in energy with $\angle(N_1–C_2–C_3–N_2) = 8.7°$. Overall, these results show that both dinuclear complexes are quite flexible and probably exhibit several energetically close minima at the S_0 potential energy surface (PES). This conformational freedom is expected to be suppressed in solid state restoring and hypsochromically shifting the emission.

For both complexes the lowest unoccupied molecular orbital (LUMO) and LUMO+1 are two combinations of π* with quinoidal character and located on ligand L1 and resemble those of pro-ligand L1 (*cf.* Figure 7 and Figure S38–S39). On the other hand, the highest occupied molecular orbital (HOMO) and HOMO-1 consist of two almost degenerate antibonding Cu–P orbitals with dπ(Cu) character. The HOMO-2 is delocalized over the whole π system of the ligand L1.

The corresponding absorption spectra were computed by means of time-dependent DFT (TD-DFT), and the resulting spectra are depicted in Figure S40, in excellent agreement with the experimental ones. The spectrum of L1 presents an intense band at 405 nm corresponding to the $S_0 \rightarrow S_1$ transition with intraligand (^{1}IL) character in agreement with the experimental data as shown by the electron density difference maps (EDDMs) in Figure S41 (*cf.* Table 2 and Table S11). The second band between 250 to 350 nm is due to the convolution of several singlet-manifold excitations, the most intense being $S_0 \rightarrow S_{13}$ computed at 267 nm. This electronic transition displays intraligand charge transfer (ICT) character with $π_{Ph} \rightarrow π^*_{TzTz}$ nature involving an electron density displacement from the terminal phenyl rings to the TzTz core of ligand L1. Conformation of ligand L1 and rotation about the $C_5–C_6$ and $C_5–C_{6'}$ bonds is further investigated in terms of energetics and optical properties highlighting the crucial role played by geometrical distortion

LUMO+1
-2.830 eV

LUMO
-3.647 eV

HOMO
-6.547 eV

HOMO-1
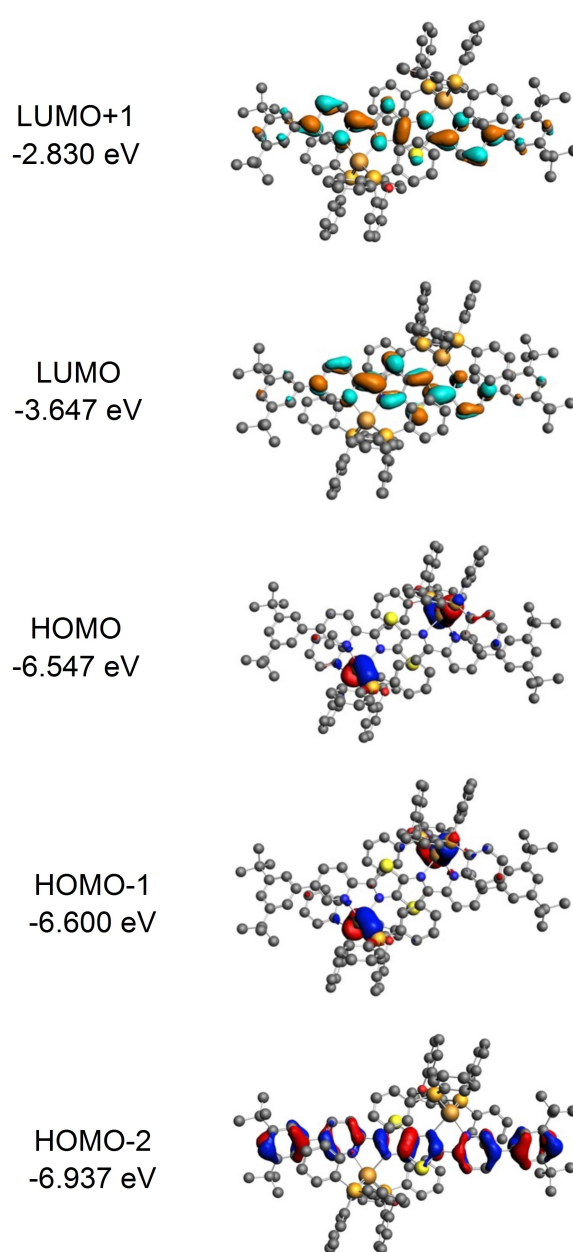**-6.600 eV**

HOMO-2
-6.937 eV

Figure 7. Nature and energies of the frontier molecular orbitals of Cu–NIR1 complex. Hydrogens are omitted for clarity.

on the optical properties in such flexible structure (see Supporting Information Discussion #3).

For both complexes Cu–NIR1 and Cu–NIR2, a first weak band is computed around 525 nm corresponding to the $S_0 \rightarrow S_1$ transition with a ^{1}MLCT dπ(Cu)$\rightarrow π^*_{TzTz}$ character (S_1 in Table S14) and symmetrically involving both [Cu(N^N)-(P^P)]$^+$ fragments at Franck–Condon (FC) geometry (Figure 8). At higher energy, both complexes present a very intense band between 400 and 450 nm in the experimental spectrum (see Figure 4), which possesses slightly different character for complex Cu–NIR1 and Cu–NIR2. For the former, this band is computed at 433 nm and associated to the $S_0 \rightarrow S_3$ with mainly ^{1}IL character involving ligand L1 and
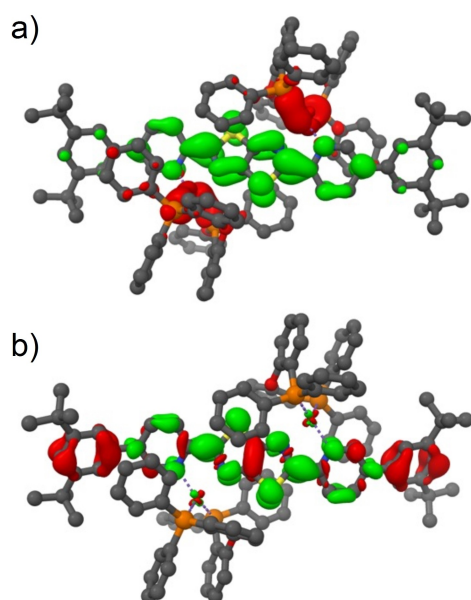
a)

b)

Figure 8. EDDMs computed between ground and excited state for $S_0 \rightarrow S_1$ (a) and $S_0 \rightarrow S_3$ (b) transition for complexes Cu–NIR1. Electronically enriched and depleted areas are colored in green and red, respectively. Hydrogens are omitted for clarity.

a)

b)

Figure 9. EDDMs computed for T_{1a} (^{3}MLCT, box a) and T_{1b} (^{3}IL, box b) state for complex Cu–NIR1 determined by electron density difference between ground and excited state. Electronically enriched and depleted areas are colored in green and red, respectively. Hydrogens are omitted for clarity.

very small ^{1}MLCT contribution (Figure 8 and S43). For Cu–NIR2, the band is the convolution of three energetically close electronic transitions at 449 nm ($S_0 \rightarrow S_5$, $\pi_{TzTz} \rightarrow \pi^*_{TzTz}$), 427 nm ($S_0 \rightarrow S_6$, ^{1}ML$_{TzTz}$CT) and 413 nm ($S_0 \rightarrow S_7$, ^{1}ML$_{TzTz}$CT) with highly mixed character (Figure S44). The higher energy band computed between 300 to 325 nm in both complexes is due to several transitions with mixed character involving significant contribution of the diphosphine. These electronic processes can be described as ligand-to-ligand charge transfer (^{1}LLCT) with $\pi_{PPh} \rightarrow \pi^*_{TzTz}$ character.

At a second stage, optimization of the lowest triplet states was carried out for both bimetallic complexes as well as the lowest singlet state (S_1) for pro-ligand L1. For the latter, details can be found in Supporting Information Discussion #3. Optimization of T_1 state of the complexes leads to two different electronic states. Starting from the FC point, optimization yields a symmetry-breaking of T_1 and localization of the MLCT manifold on one of the two [Cu(N^N)(P^P)]$^+$ fragments (hereafter referred as T_{1a} state, see Figure 8 for Cu–NIR1). This state has a two-fold degeneracy. A second minimum is found that corresponds to ^{3}IL state, hereafter called T_{1b} state, with mainly $^3\pi$-π^* character localized on the ligand L1 scaffold and showing negligible contribution of the [Cu(P^P)]$^+$ fragment (Figure 9). The geometries of the lower-lying excited states retain a highly distorted structure like that found for the GS (Tables S9 and S10). It is worth to notice that for T_{1a} minima, flattening is observed around the Cu^I where excitation is localized by ca. 15° as defined by the angle between the plane containing (Cu, P, P) and (Cu, N, N). The emission arising from both the T_{1a} and T_{1b} state are computed in the NIR domain and the values are listed in Table S15. On a model system Cu–NIR1-Me, in which the
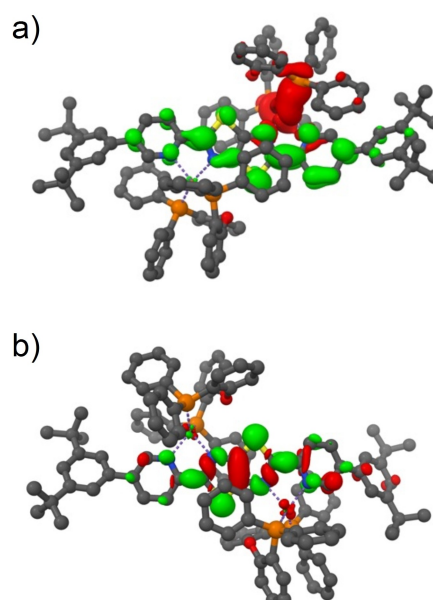
tert-Bu moieties were replaced by Me groups, optimization of the ^{1}LC state within C_i symmetry yields an emission wavelength of 528 nm. This finding strongly suggests that the transitory emission experimentally observed at 550 nm might arise from a higher-lying ^{1}LC state.

Emission arising from the T_{1a} state with ^{3}MLCT character is computed at 938 and 954 nm for derivative Cu–NIR1 and Cu–NIR2, respectively, and such state lies lower in energy than T_{1b}. For the latter manifold, emission is computed at shorter wavelength being the value 805 and 839 nm for Cu–NIR1 and Cu–NIR2, respectively. The shift between the theoretical values and the experimental ones can be due to the large geometrical flexibility that characterizes these complexes and their strong tendency to adopt a distorted geometry to maximize interligand π-stacking interactions. As abovementioned and demonstrated for pro-ligand L1 (see Supporting Information), these large geometrical distortions might sizably affect the computed emission values making one static picture alone not enough to obtain quantitative agreement. Hence, it requires an in-depth conformational analysis and Boltzmann averaged distribution of emission energies that will be reported in due course.

Besides, it should be pointed out that the computed energy difference between the T_{1a} and T_{1b} states is small, especially for Cu–NIR2 for which the difference is found to be only 35 meV, a value that is comparable to thermal energy (25 meV). Despite these differences in computed emission wavelengths, theoretical results show that the lowest triplet PES possesses close-lying minima ascribed to state with either ^{3}IL or ^{3}MLCT character. This finding is consistent with the experimental steady-state emission

profile that is described as arising from a ^{3}MLCT state. A more rigid environment, such as either solid state or glassy matrix, destabilizes energetically the ^{3}MLCT state and constrains the structure by limiting large distortions. This rigidochromic effect yields to a switch of the nature of the lowest-lying excited state that becomes now the ^{3}IL manifold in agreement with the hypsochromic shift observed in emission spectra at low temperature (see photophysical section). Similarly, rigidification of the environment in the solid state establishes interligand π-π interactions and restores NIR luminescence.

Electroluminescent characteristics of LECs

The LECs employing complexes Cu–NIR1 and Cu–NIR2 were fabricated and measured to test their EL properties. The EL characteristics of these LECs are summarized in Table S16. The EL spectra of the LECs based on complexes Cu–NIR1 and Cu–NIR2 are depicted in Figure S45. Both complexes showed similar thickness-dependent evolution in EL spectra, despite the fact that complex Cu–NIR1 shows slightly red-shifted EL emission. The thinnest LECs (ca. 70–80 nm) exhibited deep-red EL spectra ($\lambda_{max} > 650$ nm). With thickened emissive layer (ca. 150–160 nm), the EL spectra shifted to the NIR spectral region ($\lambda_{max} > 730$ nm). Further increasing the emissive-layer thickness (ca. 270–280 nm) shifted the EL spectra back to the shorter-wavelength spectral region. Thickness-dependent EL spectra of these LECs result from the modified microcavity effect upon adjusting the device optical structure.[21] These data reveal that adjusting the device thickness is essential in obtaining more NIR EL emission from these LECs. To the best of our knowledge, this work demonstrates the first NIR LECs based on copper complexes.

The device current density, light output power, and external quantum efficiency (EQE) of the LECs based on complex Cu–NIR1 and Cu–NIR2 are shown in Figure S46 and S47, respectively. The bias voltage for each device with different thickness was chosen to obtain the optimized device efficiency. After a bias was applied, the mobile ions in the emissive layer of the LEC drifted toward electrodes and lead to gradually formed electrochemically *p*- and *n*-type doped layers. These doped layers facilitated carrier injection and thus the device current increased with time. The device current decreased rapidly after reaching the peak value possibly due to the increased resistance of degraded material. The light output power initially followed the increasing device current. However, the light output power decreased faster than the device current. In addition to the material degradation, exciton quenching due to the extending doped layers toward the emission zone was responsible for reducing light output power before the device current was decreasing.[22] Owing to the improved device carrier balance induced by the growing doped layers, the EQE increased rapidly after a bias was applied. After reaching the peak value, the EQE decreased gradually due to the same reasons responsible for the reduction in the light output power with time. Among the LECs based on

complex Cu–NIR1 under test, the optimized emissive-layer thickness was 151 nm and the peak EQE reached 0.32 %. LECs based on complex Cu–NIR2 showed similar temporal evolution trend in the EL characteristics, yet with lower peak EQE (Figure S47). These EL characteristics confirm that the LECs employing the proposed copper complexes can offer NIR EL emission with moderate device efficiency. For comparison, the LECs based on complexes M1 and M2 were also fabricated. The EL characteristics of these LECs are summarized in Table S16. The EL spectra of the LECs based on complexes M1 and M2 are shown in Figure S48. The EL emission peaks of the LECs based on M1 and M2 were 666–716 and 664 nm, respectively. Compared to the EL spectra of the LECs based on the binuclear complexes with similar thicknesses (Figure S45), the mononuclear complexes showed hypsochromic shifts in the EL spectra due to shorter π-conjugation length of the chromophoric ligands. It is worth noticing that complex M1 showed time-dependent EL spectrum since the moving recombination zone in the LEC altered the microcavity effect, moving deep-red emission toward NIR region.[21]

The device current density, light output power, and EQE of the LECs based on complex M1 and M2 are shown in Figure S49 and S50, respectively. The temporal evolution trends of the EL characteristics of the LECs based on mononuclear and binuclear complexes were similar. However, lower voltages were required for the LECs based on mononuclear complexes to reach similar or even higher light output power. Since the mononuclear complexes exhibit higher energy gaps than the binuclear complexes, lower driving voltages of the LECs based on mononuclear complexes may be attributed to higher carrier mobilities of thin films of mononuclear complexes. Furthermore, the mononuclear complexes showed higher device EQEs than the binuclear complexes (Table S16). These results are consistent with the higher thin-film PLQYs of mononuclear complexes (Table S8). Without the influence of microcavity effect, both mononuclear complexes show deep-red EL emissions and thus were not used in the host–guest approach (see below) for further improving device efficiency.

To further enhance the device efficiency, both complexes were mixed with the yellow complex YIr[23] to improve the device carrier balance (see Figure S51 for chemical structure). The bias voltage for the device with a given doping concentration of complex YIr was chosen to reach the optimal device efficiency. The EL characteristics of the LECs based on either complexes Cu–NIR1 or Cu–NIR2 doped with complex YIr are summarized in Table 3. The LECs based on complex YIr have been shown to have superior device carrier balance and higher EQE.[23] Incorporating a material with better carrier balance in the emissive layer can help to balance the number of carriers.[24] However, some EL properties are altered simultaneously upon doping. The EL spectra of the LECs based on complexes Cu–NIR1 and Cu–NIR2 doped with various complex YIr concentrations are shown in Figure 10. When doped with complex YIr, the EL emission of both complexes showed hypsochromic shift due to reduced intermolecular interactions,[25] especially for higher doping concentrations

Table 3: Summary of the EL characteristics of the LECs based on complex Cu–NIR1 or Cu–NIR2 (80-x wt.%), complex YIr (x wt.%), and [BMIM$^+$ (PF$_6$)$^-$] (20 wt.%).

| complex	x_{YIr} (wt.%) [a]	Thickness [nm] [b]	Bias [V]	EL$_{max}$ [nm] [c]	L_{max} [μW cm^{-2}] [d]	$\eta_{ext, max}$ (%) [e]	$\eta_{P, max}$ [mW W^{-1}] [f]
Cu–NIR1	0	151	5	747	7.48	0.32	1.07
	8	139	4	756	7.24	0.37	1.56
	12	139	3	714	6.85	0.42	2.38
	16	134	2.5	707	2.01	0.43	2.98
	20	131	2.2	692	0.64	0.70	5.61
Cu–NIR2	0	160	8	733	5.65	0.17	0.37
	8	160	3	749	0.83	0.22	1.24
	12	150	3	718	1.28	0.24	1.41
	16	145	2.5	714	0.54	0.26	1.78

[a] Weight percentage of the complex YIr. [b] Emissive layers spin coated from the mixed solution with concentration of 60 mg mL^{-1}. [c] Stabilized EL emission peak wavelength. [d] Maximal light output power. [e] Maximal external quantum efficiency. [f] Power efficiency.
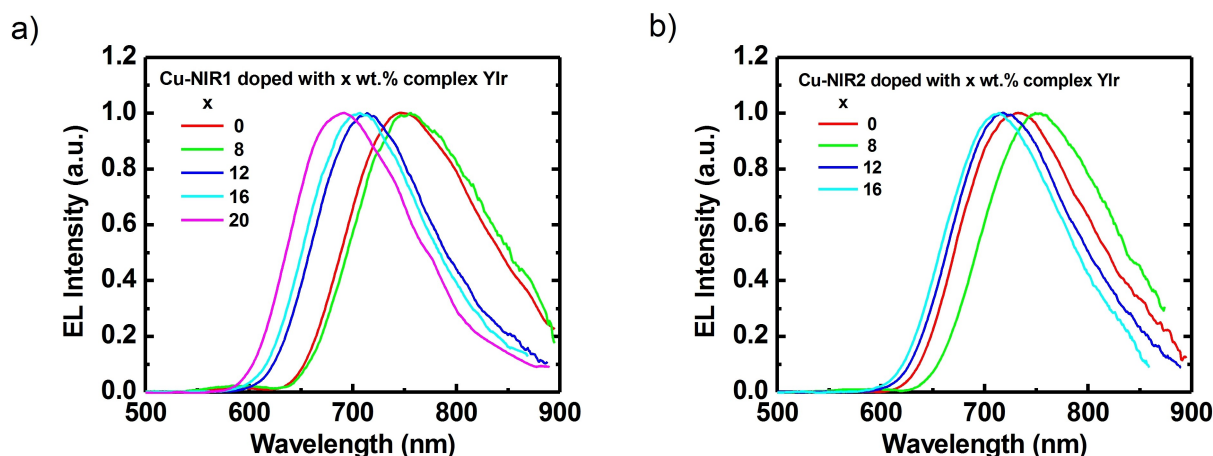
Figure 10. Doping-concentration-dependent EL spectra of the LECs based on complexes (a) Cu–NIR1 and (b) Cu–NIR2 doped with x wt.% complex YIr.

of YIr complex. To maintain the EL emission peak wavelength longer than 700 nm, the concentration of complex YIr is kept below 20 wt.%.

In addition to EL spectra, carrier transport properties in the LECs can be modified by incorporating complex YIr.[23] The device current density, light output power, and EQE of the LECs based on complex Cu–NIR1 doped with various

concentrations of complex YIr are shown in Figure 11. The bias voltage for each LEC with different complex YIr concentration was chosen to obtain the optimized device efficiency. When doped with complex YIr, comparable device current and light output power can be obtained under a lower bias voltage. It reveals improved carrier transport properties of the mixed emissive layer. Furthermore, more
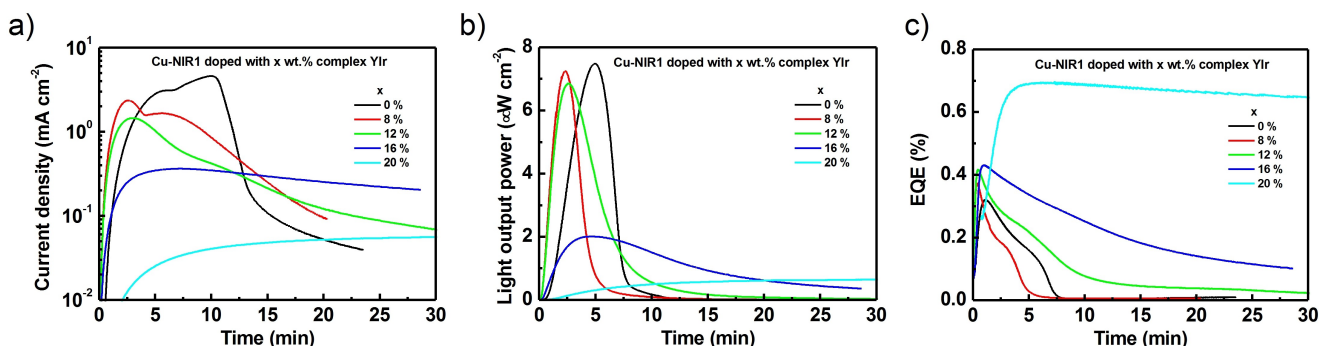
Figure 11. Time-dependent (a) current density, (b) light output power, and (c) EQE of the LECs based on complex Cu–NIR1 doped with x wt.% complex YIr. The bias voltages for the LECs doped with 0, 8, 12, 16, and 20 wt.% complex YIr are 5, 4, 3, 2.5 and 2.2 V, respectively.

balanced electrons and holes in the device enhanced the EQEs of the NIR LECs based on complex Cu–NIR1 by 34 %. The peak EQE for NIR EL ($\lambda_{max} = 707$ nm, 16 wt.% complex YIr) was 0.43 % while the peak EQE can be further increased to 0.7 % for deep-red EL ($\lambda_{max} = 692$ nm, 20 wt.% complex YIr). Similarly, doping of complex YIr also improved the carrier transport properties and carrier balance of the LECs based on complex Cu–NIR2 (see Figure S52). The peak EQE reached 0.26 %, which is enhanced by 53 % ($\lambda_{max} = 714$ nm, 16 wt.% complex YIr). As such, the proposed doping strategy is effective in further enhancing the device performance of these NIR LECs.

Inspired by the fact that the EL emissions of the proposed complexes show hypsochromic shift when the intermolecular interactions are reduced, red EL emission can be harvested by doping low-concentration NIR complex in a higher-gap host. Based on this concept, white LECs (188 nm) based on the blue-green complex B[26] doped with 0.6 wt.% complex Cu–NIR1 were fabricated and their EL characteristics were measured (see supplementary discussion #4 for further details). With the aid of efficient host complex B, the peak EQE of the white LEC reached 1.78 %, which is higher than that of the LEC employing complex Cu–NIR1. The Commission Internationale de l'Éclairage (CIE) 1931 coordinate of the stabilized EL spectra approached the equal-energy point (0.33, 0.33). These results reveal that the proposed copper complex is not only suitable for NIR LECs, but also useful in white LECs.

Conclusion

A series of binuclear cationic Cu^I complexes is disclosed that displays photoluminescence into the NIR region in solution with maximum centered at 746 nm. Despite the hypscochromic shift observed going from solution to solid state samples, for the herein presented binuclear complexes NIR emission is still preserved in the solid state. This emission was achieved thanks to a dinuclearisation strategy and establishment of two π-π stacking interligand interactions that provide a doubly locked architecture, disfavoring large excited state geometrical distortion as confirmed by single-crystal X-ray. No such π-stacking is present in the parental mononuclear counterparts. The radiative process is assigned to a long-lived excited state with ^{3}MLCT character as supported by in depth photophysical and computational analysis. Despite the PLQY values are still modest, they are amongst the highest for Cu^I derivatives in this spectral region, which prompted their successful use as EL materials in LECs devices. NIR electroluminescence was demonstrated in LECs fabricated comprising an EML with either neat binuclear Cu^I complexes or by doping a wider band gap host with the NIR emitting Cu^I as the guest. The so-fabricated LECs achieved EL maximum wavelength up to 756 nm and peak EQE of 0.43 %. Owing to the possibility to tune the EL spectral feature via EML thickness variation, a white-emitting LEC was demonstrated as well using a blue-red two component approach. To the best of our knowledge, this work demonstrated for the first time the possibility to

achieve challenging NIR EL by using earth-abundant metal complexes.

Supporting Information

The authors have cited additional references within the Supporting Information. Cartesian coordinates of the optimized structures are provided as .xyz file.

Conflict of Interest

The authors declare no conflict of interest.

Data Availability Statement

The data that support the findings of this study are available from the corresponding author upon reasonable request.

[1] S. B. Meier, D. Tordera, A. Pertegás, C. Roldán-Carmona, E. Ortí, H. J. Bolink, *Mater. Today* **2014**, *17*, 217.

[2] A. F. Henwood, E. Zysman-Colman, *Top. Curr. Chem.* **2016**, *36*, 374.

[3] O. S. Wenger, *J. Am. Chem. Soc.* **2018**, *140*, 13522; C. Förster, K. Heinze, *Chem. Soc. Rev.* **2020**, *49*, 1057.

[4] a) G. U. Mahoro, J. Fernandez-Cestau, J. Renaud, P. B. Coto, R. D. Costa, S. Gaillard, *Adv. Opt. Mater.* **2020**, *8*, 2000260; b) C. E. Housecroft, E. C. Constable, *J. Mater. Chem. C* **2022**, *10*, 4456; c) D. Volz, M. Wallesch, C. Fléchon, M. Danz, A. Verma, J. M. Navarro, D. M. Zink, S. Bräse, T. Baumann, *Green Chem.* **2015**, *17*, 1988.

[5] a) M. D. Weber, E. Fresta, M. Elie, M. E. Miehlich, J.-L. Renaud, K. Meyer, S. Gaillard, R. D. Costa, *Adv. Funct. Mater.* **2018**, *28*, 1707423; b) M. Elie, F. Sguerra, F. Di Meo, M. D. Weber, R. Marion, A. Grimault, J.-F. Lohier, A. Stallivieri, A. Brosseau, R. B. Pansu, J.-L. Renaud, M. Linares, M. Hamel, R. D. Costa, S. Gaillard, *ACS Appl. Mater. Interfaces* **2016**, *8*, 14678; c) H. Ohara, A. Kobayashi, M. Kato, *Dalton Trans.* **2014**, *43*, 17317; d) S. Brown-Xu, M. Fumanal, C. Gourlaouen, L. Gimeno, A. Quatela, C. Thobie-Gautier, E. Blart, A. Planchat, F. Riobé, C. Monnereau, L. X. Chen, C. Daniel, Y. Pellegrin, *Inorg. Chem.* **2019**, *58*, 7730; e) L. Gimeno, B. T.

Phelan, E. A. Sprague-Klein, T. Roisnel, E. Blart, C. Gourlaouen, L. X. Chen, Y. Pellegrin, *Inorg. Chem.* **2022**, *61*, 7296; f) N. Armaroli, G. Accorsi, M. Holler, O. Moudam, J.-F. Nierengarten, Z. Zhou, R. T. Wegh, R. Welter, *Adv. Mater.* **2006**, *18*, 1313; g) L. Gimeno, E. Blart, J. Rebilly, M. Coupeau, M. Allain, T. Roisnel, A. Quarré de Verneuil, C. Gourlaouen, C. Daniel, Y. Pellegrin, *Chem. Eur. J.* **2020**, *26*, 11887; h) T. Phan, N. Armaroli, A. Saavedra Moncada, E. Bandini, B. Delavaux-Nicot, J. Nierengarten, D. Armspach, *Angew. Chem. Int. Ed.* **2023**, *62*, e202214638.

[6] a) M. Wallesch, D. Volz, D. M. Zink, U. Schepers, M. Nieger, T. Baumann, S. Bräse, *Chem. Eur. J.* **2014**, *20*, 6578; b) K. Tsuge, Y. Chishina, H. Hashiguchi, Y. Sasaki, M. Kato, S. Ishizaka, N. Kitamura, *Coord. Chem. Rev.* **2016**, *306*, 636.

[7] P. C. Ford, E. Cariati, J. Bourassa, *Chem. Rev.* **1999**, *99*, 3625.

[8] a) B. Hupp, C. Schiller, C. Lenczyk, M. Stanoppi, K. Edkins, A. Lorbach, A. Steffen, *Inorg. Chem.* **2017**, *56*, 8996; b) M. Gernert, L. Balles-Wolf, F. Kerner, U. Müller, A. Schmiedel, M. Holzapfel, C. M. Marian, J. Pflaum, C. Lambert, A. Steffen, *J. Am. Chem. Soc.* **2020**, *142*, 8897; c) A. M. T. Muthig, M. Krumrein, J. Wieland, M. Gernert, F. Kerner, J. Pflaum, A. Steffen, *Inorg. Chem.* **2022**, *61*, 14833.

[9] R. Hamze, J. L. Peltier, D. Sylvinson, M. Jung, J. Cardenas, R. Haiges, M. Soleilhavoup, R. Jazzar, P. I. Djurovich, G. Bertrand, M. E. Thompson, *Science* **2019**, *363*, 601.

[10] Y. Jeon, H.-R. Choi, K.-C. Park, K. C. Choi, *J. Soc. Inf. Display* **2020**, *28*, 324.

[11] E. Fresta, M. D. Weber, J. Fernandez-Cestau, R. D. Costa, *Adv. Opt. Mater.* **2019**, *7*, 1900830.

[12] a) M. Mauro, *Chem. Commun.* **2021**, *57*, 5857; b) P. Pander, A. V. Zaytsev, A. Sil, J. A. G. Williams, P. H. Lanoe, V. N. Kozhevnikov, F. B. Dias, *J. Mater. Chem. C* **2021**, *9*, 10276; c) W. Song, H. Mao, K. Shao, G. Shan, Y. Gao, Q. Zeng, F. Li, Z. Su, *J. Mater. Chem. C* **2023**, *11*, 1197; d) P. Rajakannu, W. Lee, S. Park, H. s. Kim, H. Mubarok, M. H. Lee, S. Yoo, *Adv. Funct. Mater.* **2023**, *33*, 2211853.

[13] Deposition numbers 2251525 (for **NIR-Cu1**) and 2251639, 2251640, 2251641 and 2251642 (for **NIR-Cu2**, **M1**, **M2** and **L**, respectively) contain the supplementary crystallographic data for this paper. These data are provided free of charge by the joint Cambridge Crystallographic Data Centre and Fachinformationszentrum Karlsruhe Access Structures service.

[14] a) K. Saito, T. Tsukuda, T. Tsubomura, *Bull. Chem. Soc. Jpn.* **2006**, *79*, 437; b) A. Kaeser, M. Mohankumar, J. Mohanraj, F. Monti, M. Holler, J.-J. Cid, O. Moudam, I. Nierengarten, L. Karmazin-Brelot, C. Duhayon, B. Delavaux-Nicot, N. Armaroli, J.-F. Nierengarten, *Inorg. Chem.* **2013**, *52*, 12140; c) C.-W. Hsu, C.-C. Lin, M.-W. Chung, Y. Chi, G.-H. Lee, P.-T. Chou, C.-H. Chang, P.-Y. Chen, *J. Am. Chem. Soc.* **2011**, *133*, 12085.

[15] E. Leoni, J. Mohanraj, M. Holler, M. Mohankumar, I. Nierengarten, F. Monti, A. Sournia-Saquet, B. Delavaux-Nicot, J.-F. Nierengarten, N. Armaroli, *Inorg. Chem.* **2018**, *57*, 15537.

[16] A. J. Bard, L. R. Faulkner, *Electrochemical Methods, Fundamentals and Applications*, 2nd ed., Wiley, New York, **2001**.

[17] K. M. Omer, S.-Y. Ku, A. J. Bard, *Angew. Chem. Int. Ed.* **2009**, *48*, 9300–9303.

[18] M. Iwamura, S. Takeuchi, T. Tahara, *Acc. Chem. Res.* **2015**, *48*, 782.

[19] a) A. Jouaiti, V. Giuso, C. Cebrián Ávila, P. Mercandelli, M. Mauro, *Dyes Pigm.* **2022**, *208*, 110780; b) M. R. Pinto, Y. Takahata, T. D. Z. Atvars, *J. Photochem. Photobiol. A* **2001**, *143*, 119; c) A. N. Woodward, J. M. Kolesar, S. R. Hall, N.-A. Saleh, D. S. Jones, M. G. Walter, *J. Am. Chem. Soc.* **2017**, *139*, 8467.

[20] M. J. Leitl, D. M. Zink, A. Schinabeck, T. Baumann, D. Volz, H. Yersin, *Top. Curr. Chem.* **2016**, *374*, 25.

[21] a) J.-H. Hsu, H.-C. Su, *Phys. Chem. Chem. Phys.* **2016**, *18*, 5034; b) Z. Yang, H. Su, *Adv. Funct. Mater.* **2020**, *30*, 1906788.

[22] S. van Reenen, R. A. J. Janssen, M. Kemerink, *Adv. Funct. Mater.* **2015**, *25*, 3066.

[23] R.-H. Yi, C.-L. Lo, D. Luo, C.-H. Lin, S.-W. Weng, C.-W. Lu, S.-W. Liu, C.-H. Chang, H.-C. Su, *ACS Appl. Mater. Interfaces* **2020**, *12*, 14254.

[24] P.-C. Huang, G. Krucaite, H.-C. Su, S. Grigalevicius, *Phys. Chem. Chem. Phys.* **2015**, *17*, 17253; H.-F. Chen, C.-T. Liao, H.-C. Su, Y.-S. Yeh, K.-T. Wong, *J. Mater. Chem. C* **2013**, *1*, 4647.

[25] G.-X. Yu, C.-H. Lin, Y.-X. Liu, R.-H. Yi, G.-Y. Chen, C.-W. Lu, H.-C. Su, *Chem. Eur. J.* **2019**, *25*, 13748.

[26] M.-L. Wu, G.-Y. Chen, T.-A. Shih, C.-W. Lu, H.-C. Su, *Phys. Chem. Chem. Phys.* **2018**, *20*, 18226.

[27] E. S. Barskaya, E. K. Beloglazkina, A. G. Mazhuga, I. V. Yudin, N. V. Zyk, *Russ. Chem. Bull.* **2015**, *64*, 1975–1977.

[28] M86-EXX229 V1 APEX3 User Manual, Bruker AXS Inc., Madison, USA, **2016**.

[29] G. M. Sheldrick, *Acta Crystallogr. Sect. A* **2015**, *71*, 3–8.

[30] G. M. Sheldrick, *Acta Crystallogr. Sect. A* **2015**, *71*, 3–8.

[31] a) G. A. Crosby, J. N. C. Demas, *J. Am. Chem. Soc.* **1970**, *92*, 7262; b) H. Ishida, J.-C. Bünzli, A. Beeby, *Pure Appl. Chem.* **2016**, *88*, 701; c) C. Würth, M. Grabolle, J. Pauli, M. Spieles, U. Resch-Genger, *Nat. Protoc.* **2013**, *8*, 1535.

[32] I. Ishida, S. Tobita, Y. Hasegawa, R. Katoh, K. Nozaki, *Coord. Chem. Rev.* **2010**, *254*, 2449.

[33] J. R. Lakowicz, in *Principles of Fluorescence Spectroscopy*, 3rd ed., Springer, New York, **2006**, p. 141.

[34] G. te Velde, F. M. Bickelhaupt, E. J. Baerends, C. Fonseca Guerra, S. J. A. van Gisbergen, J. G. Snijders, T. Ziegler, *J. Comput. Chem.* **2001**, *22*, 931.

[35] P. J. Stephens, F. J. Devlin, C. F. Chabalowski, M. J. Frisch, *J. Phys. Chem.* **1994**, *98*, 11623.

[36] E. Van Lenthe, E. J. Baerends, *J. Comput. Chem.* **2003**, *24*, 1142.

[37] E. van Lenthe, A. Ehlers, E.-J. Baerends, *J. Chem. Phys.* **1999**, *110*, 8943.

[38] S. Grimme, J. Antony, S. Ehrlich, H. Krieg, *J. Chem. Phys.* **2010**, *132*, 154104.

[39] C. C. Pye, T. Ziegler, *Theor. Chem. Acc.* **1999**, *101*, 396.

[40] S. J. A. van Gisbergen, J. G. Snijders, E. J. Baerends, *Comput. Phys. Commun.* **1999**, *118*, 119.

[41] F. Wang, T. Ziegler, *J. Chem. Phys.* **2005**, *123*, 154102.

[42] S. Hirata, M. Head-Gordon, *Chem. Phys. Lett.* **1999**, *314*, 291.

[43] F. Plasser, *J. Chem. Phys.* **2020**, *152*, 084108.

[44] M. Kohout, *DGrid*, version 4.5, Radebeul, **2009**.

[45] J. Contreras-García, E. R. Johnson, S. Keinan, R. Chaudret, J.-P. Piquemal, D. N. Beratan, W. Yang, *J. Chem. Theory Comput.* **2011**, *7*, 625.

[46] S. Antonello, M. Musumeci, D. D. M. Wayner, F. Maran, *J. Am. Chem. Soc.* **1997**, *119*, 9541.

[47] A. B. Meneses, S. Antonello, M. C. Arévalo, F. Maran, *Electroanalysis* **2006**, *18*, 363.

[48] Y.-Z. Chen, D. Luo, C.-H. Hsiang, R.-H. Yi, C.-H. Lin, C.-W. Lu, S.-W. Liu, C.-H. Chang, H.-C. Su, *Org. Electron.* **2020**, *77*, 105515.

[49] H.-C. Su, H.-F. Chen, Y.-C. Shen, C.-T. Liao, K.-T. Wong, *J. Mater. Chem.* **2011**, *21*, 9653.

[50] Y. Chen, Y.-X. Wang, C.-W. Lu, H.-C. Su, *J. Mater. Chem. C* **2022**, *10*, 11211.
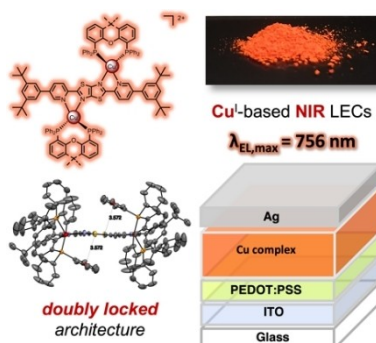
Research Articles

Light-Emitting Electrochemical Cells

A. Jouaiti,* L. Ballerini, H.-L. Shen, R. Viel,
F. Polo, N. Kyritsakas, S. Haacke, Y.-
T. Huang, C.-W. Lu, C. Gourlaouen, H.-
C. Su,* M. Mauro* —————— **e202305569**

Binuclear Copper(I) Complexes for Near-Infrared Light-Emitting Electrochemical Cells

A series of near-infrared emitting (NIR) compounds based on earth-abundant binuclear Cu^I complexes is presented. Two π-stacking interactions are found in their solid-state structure yielding to doubly locked architectures that help to suppress excited state flattening distortions and quenching. The complexes have been successfully used in light-emitting electrochemical cells (LECs), and unprecedented NIR electroluminescence (EL) with Cu^I compounds was achieved.